doi:10.1038/nature06052

ARTICLES

Structural insight into filament formation by mammalian septins

Minhajuddin Sirajuddin[1], Marian Farkasovsky[1]†, Florian Hauer[2], Dorothee Kühlmann[1], Ian G. Macara[3], Michael Weyand[1], Holger Stark[2] & Alfred Wittinghofer[1]

Septins are GTP-binding proteins that assemble into homo- and hetero-oligomers and filaments. Although they have key roles in various cellular processes, little is known concerning the structure of septin subunits or the organization and polarity of septin complexes. Here we present the structures of the human SEPT2 G domain and the heterotrimeric human SEPT2–SEPT6–SEPT7 complex. The structures reveal a universal bipolar polymer building block, composed of an extended G domain, which forms oligomers and filaments by conserved interactions between adjacent nucleotide-binding sites and/or the amino- and carboxy-terminal extensions. Unexpectedly, X-ray crystallography and electron microscopy showed that the predicted coiled coils are not involved in or required for complex and/or filament formation. The asymmetrical heterotrimers associate head-to-head to form a hexameric unit that is nonpolarized along the filament axis but is rotationally asymmetrical. The architecture of septin filaments differs fundamentally from that of other cytoskeletal structures.

Septins are conserved GTP-binding proteins discovered in the budding yeast *Saccharomyces cerevisiae*, where they organize into a ring at the bud neck[1–4]. A parallel array of filaments is formed from hetero-oligomers of four septins, which interact asymmetrically with other proteins during cell division[5,6]. The 13 human septin genes can be subdivided into 4 groups, which can, in principle, generate dozens of redundant heteromeric complexes[7–9]. They have key roles in cell division, cytoskeletal dynamics and secretion[10], and have been implicated in the pathogenesis of various diseases including neoplasia and neurodegenerative conditions[11]. Missense *SEPT9* mutations were recently found to be responsible for hereditary neuralgic amyotrophy[12].

Not much is known about the structure of septins, the role of guanine nucleotide binding and GTP hydrolysis in septin function[13]. Mammalian septin complexes isolated from brain tissue or HeLa cells contain between three–five major isoforms[14–17]. Purified septin complexes from *S. cerevisiae* with Cdc3–Cdc10–Cdc11–Cdc12 and from *Drosophila* with Pnut–Sep1–Sep2 have 2:2:2:2 and 2:2:2 stoichiometries[18–20], and contain 1 mol guanine nucleotide per polypeptide[20–22]. Recombinant mammalian and yeast complexes with different numbers of septins contain bound nucleotides with varying affinities and stoichiometries[22,23], whereas the recombinant octameric yeast complex is fully saturated with tightly bound nucleotide[21,22]. The trimeric SEPT2–SEPT6–SEPT7 complex, but not the dimeric human SEPT6–SEPT7 complex, forms filaments[23], whereas the *Caenorhabditis elegans* UNC-59 and UNC-61 gene products are sufficient for filament formation[24]. Because a single recombinant Sept2 from *Xenopus laevis* and human SEPT2 expressed in insect cells can be reconstituted into filaments, a defined number of subunits is apparently not required for filament formation[25,26]. Septin filaments have 7–9-nm width and various length, with a unit length of 25–32 nm observed under high salt concentration[3,18,20,25]. As an approach to understand septin function better, we have determined the X-ray structure of the human SEPT2 G domain and the SEPT2–SEPT6–SEPT7 complex.

The SEPT2 G domain

Human SEPT2 lacking 46 residues of the predicted C-terminal coiled coil (SEPT2-315) was isolated as recombinant protein from *Escherichia coli*. It contains 50% bound GDP and elutes in several peaks during gel filtration, two of which correspond to apparent molecular masses of 36 and 72 kDa, respectively (Fig. 1a). In the presence of GDP, GppNHp (a slowly hydrolysing GTP analogue) or alkaline phosphatase, the monomer–dimer equilibrium is shifted towards the dimer or monomer, respectively, indicating that dimerization is influenced by the presence but not the nature of the nucleotide. SEPT2-315 was crystallized in the presence of excess GDP and the structure was solved using selenomethionine single-wavelength anomalous dispersion (SAD) to a resolution of 3.4 Å (Table 1). In the asymmetrical unit of the crystal, SEPT2 is dimerized via two different interfaces (Fig. 1b).

The basic structure of monomeric SEPT2 closely resembles the canonical G domain exemplified by Ras, with six β-strands and five α-helices (Fig. 1c and Supplementary Fig. 1). A unique feature of SEPT2 is the presence of four additional elements compared to Ras. These are the N-terminal helix α0 (to preserve the canonical G domain nomenclature), α5′ between α4 and β6, the two antiparallel strands β7 and β8, and the α6 C-terminal helix that points away from the G domain at a 90° angle relative to the axis of interaction between subunits. The sequences of the additional elements are highly conserved. They contain residues that are invariant between SEPT2–SEPT6–SEPT7 and most other septins and are involved in contact to neighbouring subunits. GDP is bound in a conventional way, with the phosphates occupying the P-loop and the AKAD motif contacting the guanine base.

SEPT2 forms dimers via the nucleotide-binding site

Interface 1 of the septin dimer is along the nucleotide-binding site and forms the G-dimer, whereas interface 2 is mediated by the extra N-and C-terminal helices to form the NC-dimer (Fig. 1b and Supplementary Fig. 2a). The sizes of the interfaces are 1,851 Å^2 and

[1]Abteilung Strukturelle Biologie, Max-Planck-Institut für molekulare Physiologie, Otto-Hahn-Strasse 11, 44227 Dortmund, Germany. [2]Max-Planck-Institut für Biophysikaische Chemie, Am Fassberg 11, 37077 Goettingen, Germany. [3]Center for Cell Signaling, Department of Microbiology, University of Virginia School of Medicine, Charlottesville, Virginia 22908-0577, USA. †Present address: Institute of Molecular Biology SAS, Dubravska cesta 21, 845 51 Bratislava, Slovak Republic.

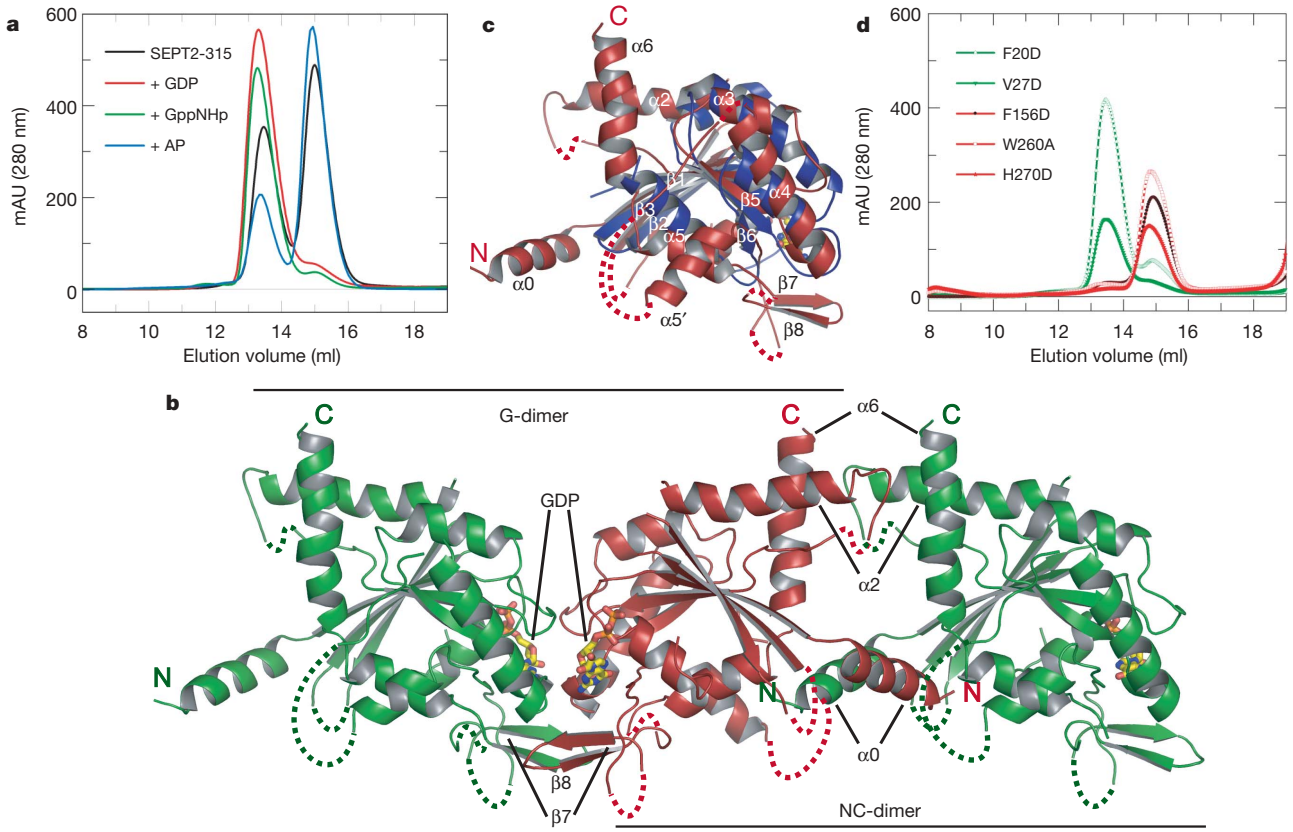

Figure 1 | Structure and dimerization of SEPT2. a, Gel filtration analysis of SEPT2-315 on a Superdex S-200 column. The elution profile shows a monomer–dimer equilibrium, which is shifted by the presence of excess GDP or GppNHp as indicated. In the presence of alkaline phosphatase (AP), which degrades nucleotides, the protein runs as a monomer predominantly. AU, absorption units. **b**, Ribbon representation of three SEPT2-315 monomers found in the crystal, with two possible dimer interfaces labelled G- or NC-dimer, as indicated. Dashed lines represent disordered regions. **c**, Superimposition of the structures of SEPT2-315 (red) and Ras–GppNHp (blue) (Protein Data Bank 121P), indicating the extra secondary structure elements of the septin G domain. **d**, Gel filtration of mutant SEPT2 variants in the presence of excess GDP, analysed as described in **a**.

2,995 Å^2 for the G-dimer and the NC-dimer, respectively. To delineate which of these represents the solution structure, we mutated residues that are likely to contribute to the binding energy and are highly conserved (Supplementary Fig. 2b).

Phenylalanine 156 of SEPT2 interacts with Phe 156 from the other SEPT2 subunit and was mutated to Asp, whereas Trp 260 and His 270, which interact, were mutated to Ala and Asp, respectively. For the NC-dimer, Val 27 and Phe 20 were mutated to Asp. Dimer formation was analysed by analytical gel filtration in the presence of GDP (Fig. 1d). Whereas mutants of the NC-dimer interface showed the same equilibrium between monomer and dimer as wild-type SEPT2, the G interface mutants eluted as monomers. These results demonstrate that SEPT2 forms dimers across the nucleotide-binding site, with a face to face orientation of nucleotide-binding sites, similar to other GTP-binding proteins of the TRAFAC and SIMIBI classes[27] such as MnmE[28] and HypB[29], consistent with our observation that saturation with nucleotide favours dimerization (Fig. 1a).

Table 1 | X-ray refinement statistics

	SEPT2-315	Human septin complex
Resolution (Å)	20–3.4	49.15–4
R_{work}/R_{free} (%)	27.9/31.3	37.5/39.2
Number of atoms		
Protein	3,650	4,575
Ligand/ion	56	87
B-factors		
Protein	80.27	78.3
Ligand	65.43	71.4
r.m.s deviations		
Bond lengths (Å)	0.012	0.057
Bond angles (°)	1.589	4.7

Structure of the human septin complex

The human septin complex consisting of full-length SEPT2–SEPT6–SEPT7 was isolated basically as described for the recombinant yeast complex[22]. Using gel filtration, the molecular mass of the complex was estimated as ~285 kDa, which accounts for a hexamer. It contains ~70% bound nucleotide relative to protein with a GDP:GTP ratio of >2:1. The structure of human septin complex was solved using the MIRAS (multiple isomorphous heavy-atom replacement using anomalous scattering) approach. The electron density reveals 4–5-nm-wide tubes, indicating that the human septin complex is polymerized under crystallization conditions (Supplementary Fig. 3). The asymmetrical unit of the crystal is a trimer rather than a hexamer. Subunit assignment of the trimer was guided by selenomethionine sites (Fig. 2a).

The final model of the SEPT2–SEPT6–SEPT7 repeating unit (Fig. 2b) shows that the filament in the crystal consists of an assembly of G domains; the G domains contact each other using the same conserved G and NC interfaces observed in the SEPT2 crystal. Surprisingly, no density is seen for the predicted C-terminal coiled coils, although there is sufficient space available between parallel filaments in the crystal. To exclude protein truncation during crystal formation, human septin complex crystals were dissolved and shown to contain full-length protein (not shown). Although the resolution of the structure is limited to 4 Å, we would expect to see density for the coiled coils because the density of the G domain is well defined. The location of the coiled coils can be deduced from the direction of helices α6, which protrude at a right angle to the filament axis and could in principle form parallel coiled coils, as predicted for SEPT6 and SEPT7 from fluorescence resonance energy transfer (FRET) data[30].

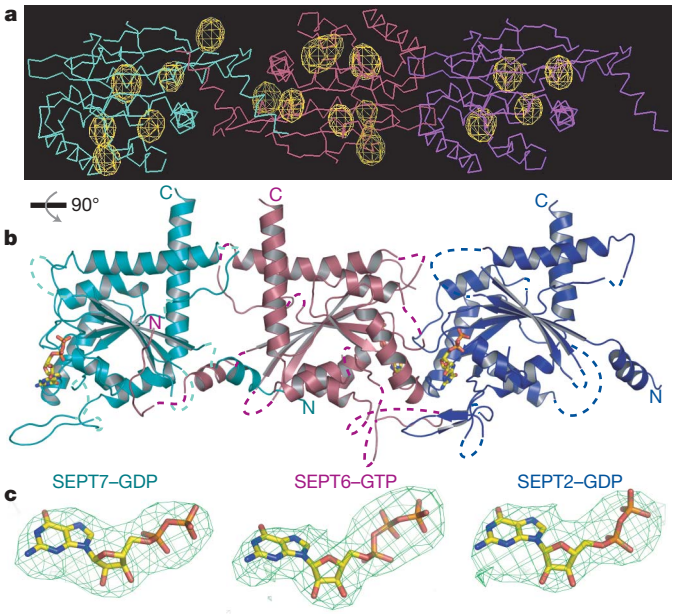

Figure 2 | Structural analysis of the human septin complex. **a**, Superimposition of the molecular replacement solution using the SEPT2 G domain onto the selenomethionine anomalous map contoured at 5σ to assign the location of the SEPT2, SEPT6 and SEPT7 subunits in the asymmetrical unit. **b**, Ribbon model of the trimeric SEPT2–SEPT26–SEPT27 complex, with SEPT7 in cyan, SEPT6 in pink and SEPT2 in blue, with nucleotides in ball and stick representation. **c**, Positive $F_o - F_c$ electron density map, contoured at 3σ, around the nucleotide-binding sites of the respective septins, and the resulting nucleotide models, as indicated.

There is a continuing debate as to whether the nature of bound nucleotide determines septin complex or filament formation, and whether GTP hydrolysis has a role in the process. Nucleotides are found in each septin active site. The $F_o - F_c$ electron densities of SEPT7 and SEPT2 are very consistent with a GDP nucleotide, whereas SEPT6 contains additional density that we tentatively assign to the γ-phosphate of GTP (Fig. 2c), consistent with biochemical findings[7,20–22].

Human septin complex is a linear hexamer

Electron microscopy of the human septin complex shows that the filament structure in the crystal also represents the structure in solution. Under low salt concentration, the heterotrimer forms filaments and rings of various dimensions with no consistent pattern. At high salt concentration, short pieces of uniform length become prevalent. Single-particle analysis shows a hexameric assembly consistent with a dimer of the trimeric asymmetrical unit of the crystal, with similar dimensions. It consists of six equally sized subunits, consistent with an array of G domains (Fig. 3a)[15]. No density corresponding to the C-terminal ends was observed after averaging. To confirm that the C termini are dispensable for complex formation, we found that a complex lacking coiled coils consisting of SEPT2(1–308), SEPT6(1–310) and SEPT7(1–305) could be isolated with the same purification procedure as wild-type human septin complex. We conclude that the coiled coils are not required for formation of a stable hexameric complex. Single-particle analysis did not reveal significant differences compared to the wild-type human septin complex (Fig. 3b).

Architecture of the hexamer

Although the electron microscopy studies show that the human septin complex forms a hexamer at high salt concentration, it is not possible to deduce, from the linear arrangement of subunits in the crystal, the boundaries of the solution particle. We thus analysed a complex between a maltose binding protein (MBP)–SEPT2 fusion and SEPT6–SEPT7, an intermediate of the purification scheme. Electron microscopy analysis (Fig. 3d) shows an extra density located at the centre of the particle. The fact that only one extra particle is

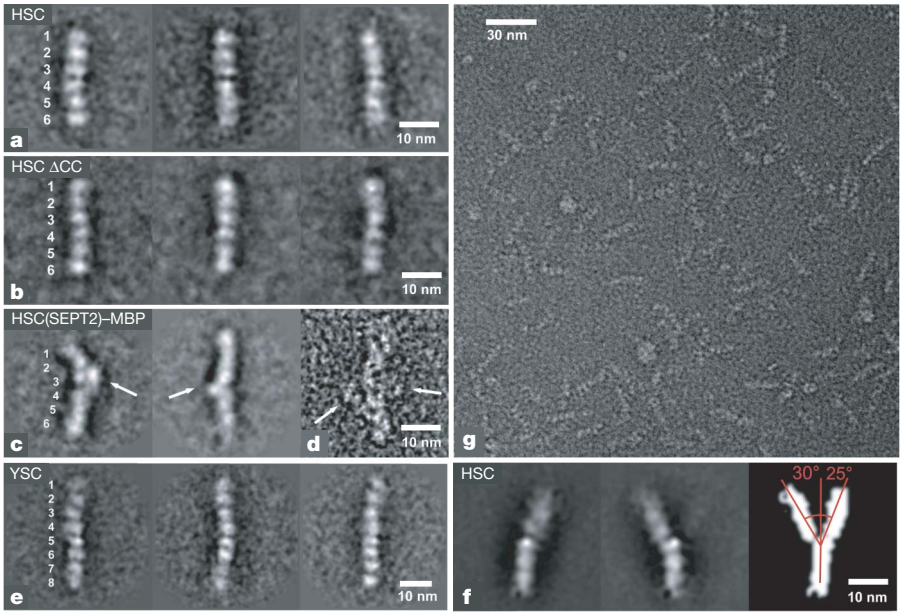

Figure 3 | Electron microscopic studies of septin complexes. **a**, Class averages of the negatively stained human septin complex (HSC) at high salt concentration obtained after reference-free alignment, MSA and classification. **b**, Class averages of the deleted coiled coil (ΔCC) human septin complex at high salt concentration showing the same hexameric arrangement and comparable density distribution as in **a**. **c**, Class averages of the MBP-fused human septin complex. Densities attributed to the fused MBP are indicated by an arrow and located close to the central part of the complex. **d**, Single-particle image of the MBP-fused human septin complex. Both MBP fusion tags are visible as lateral protrusions highlighted by the arrows. **e**, Class averages of the Cdc3–Cdc10–Cdc11–Cdc12 yeast septin complex (YSC). In contrast to the human septin complex, the yeast septin complex forms an octameric complex. **f**, Class averages after alignment of the human septin complex using only the lower trimeric part as a reference to align the raw images. The upper trimeric part adopts different orientations, indicating the high level of flexibility of the hexamer. Bending is observed in the 25–30° range around a hinge formed by the central SEPT2 dimer. **g**, Raw electron micrograph of the human septin complex at high salt concentration.

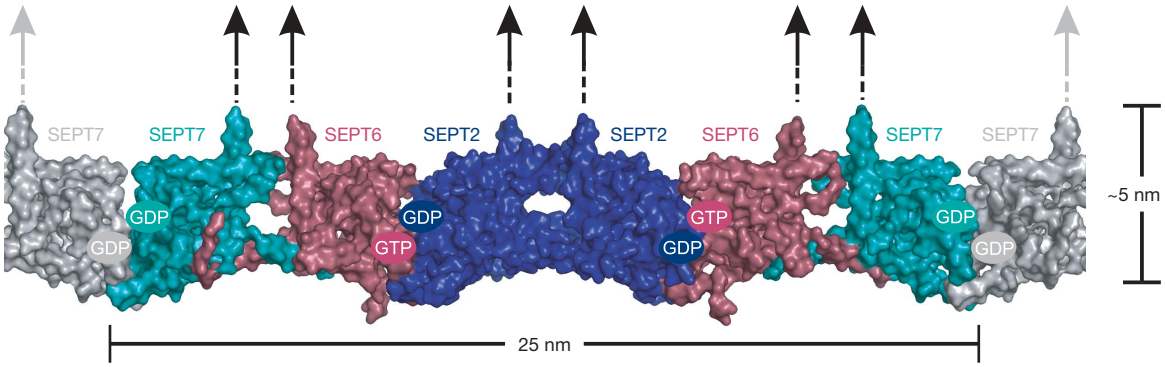

Figure 4 | The septin filament. Surface representation of the basic hexameric unit (in colour). The neighbouring hexamer makes longitudinal contact using SEPT7 (in grey), thereby forming septin filaments. The nature of the nucleotide in the subunits is indicated. The presumed orientations of the C-terminal ends predicted to form coiled coils are shown schematically.

visible instead of two in most images (Fig. 3c) might be due to the flexible connection of the tag and/or the arrangement of particles on the grid. However, in combination with the X-ray data, the evidence for an arrangement of septins in the order 7-6-2-2-6-7 is unequivocal (Fig. 4). Thus, the SEPT7–SEPT6 interaction takes place by means of the NC interface, whereas the SEPT6–SEPT2 interaction is via the G interface. Notably, the SEPT2–SEPT2 interaction favours the NC interface rather than the G interface found for the isolated SEPT2 in solution, supporting the notion that septin interactions appear fairly promiscuous. Filament formation in the crystal and most likely in solution involves a SEPT7–SEPT7 G-dimer interaction, which should be sensitive to high salt concentration, whereas the G interface between SEPT2 and SEPT6 is not, arguing that the G-dimer interface of heterodimers is differentially sensitive or tighter than the G-dimer interface of homodimers.

Bending of filaments

By aligning all human septin complex particles against a linear trimer, flexibility of the hexameric complex is revealed by multivariate statistical analysis (MSA) and classification[31,32] (Fig. 3f). Straight and kinked states are found in almost equal amounts within the particle population. The observed average flexibility of the hexamer can be described by bending one trimer with respect to the other by 25–30° around a hinge formed by the SEPT2–SEPT2 interface. This interface appears as an obvious hinge element, because it is connected by thinner density elements. Consistent with this, the upper half of the NC-dimer interface of SEPT2 near α2/6 is mediated mostly by charged residues (Fig. 1b and Supplementary Fig. 2a), which should be destabilized by the high salt concentration used in the electron microscopy analysis. This analysis indicates that septin filaments are not uniformly linear *in vitro*, consistent with observations that they can form ring-like structures *in vitro* and *in vivo*.

Discussion

The N-terminal extensions of the septin G domain upstream of α0 are usually fairly short, except for SEPT9 (also called MSF), and have no apparent secondary structure. The longer N terminus of SEPT6 makes additional contacts with SEPT7 and may thus be involved in tightening the interaction between the subunits. The C-terminal extensions have a strong coiled-coil probability and were expected to be structured and contribute to complex formation. Surprisingly, they were neither visible in the X-ray nor in the electron microscopy analyses. It could be that these regions are natively unstructured and only adopt structure by interacting with partner proteins such as the BORGs[17] or other septin filaments. Alternatively, they might indeed adopt parallel coiled-coil structures as predicted[30], but are connected to the G domain via a flexible linker. Because such a break in the coiled-coil prediction does exist (Supplementary Fig. 1), the C termini might indeed adopt numerous positions relative to the G domain and are thus not visible. Thin strands projecting outwards from a rat oligomeric septin complex have been observed before[15] and can also be identified in some of our electron microscopy images (Fig. 3g), but are lost on averaging. For the SEPT6–SEPT7 coiled coils, it was shown that they directly interact with each other[30]. Although the G domain alone is sufficient to mediate complex and filament formation, the proximity of C termini of SEPT6–SEPT7 could indicate that the coiled coils, although not required, may further stabilize filament formation, consistent with results on recombinant coiled-coil-deleted *Xenopus laevis* Sept2 (ref. 25).

The 4–5-nm width of septin filaments from our crystal and electron microscopy analyses is about half the size of 7–9-nm septin filaments described in electron microscopic studies and consistently quoted in the literature. Although the nature of the discrepancy is not obvious, two single filaments tightly packed against each other would form such a particle. Paired filaments with varying space between them have been described, and the 8-nm filament could thus be a special case. The C-terminal regions may be involved in forming paired filaments or higher order structures seen *in vitro* and *in vivo*[3,4,14,18,33]. Because C-terminal extensions of neighbouring filaments point into the same direction, the formation of paired filaments is prevented in the crystal.

The extended G domains of septins serve as universal building blocks for polymer formation, which is in contrast to published models. Polymers can be formed by a variable number of subunits using different combinations of septins. To show that this is a common design principle we analysed the recombinant yeast Cdc3–Cdc10–Cdc11–Cdc12 complex. Electron microscopy analysis shows a particle of 32-nm length and 4–5-nm width clearly composed of eight subunits (Fig. 3e), as predicted from previous biochemical analysis and consistent with the structural findings[18,22,34]. The nature of the nucleotide indicates that it might have a role in oligomer and filament formation, because we observe that in the interface between SEPT6–GTP and SEPT2–GDP the switch regions are better defined than in the SEPT7–GDP interface. The data also show that the G-dimer interface between the homodimer SEPT7–SEPT7 can be dissociated using high salt concentration, but this is not the case for the G-dimer interface between the heterodimer SEPT6–SEPT2, possibly due to the nature of bound nucleotide. To decipher the rules of complex and filament formation, the role of nucleotide binding and GTP hydrolysis, and the function of the C-terminal extensions, more biochemical experiments and structural studies, possibly with higher resolutions, will be required. The structures presented here will provide powerful tools for the design of appropriate experiments.

METHODS SUMMARY

SEPT2-315 was isolated from *E. coli* using the glutathione *S*-transferase (GST) tag. Analytical gel filtration of SEPT2-315 was performed over a Superdex S-200

10/30 column (Amersham) with an ÄKTA explorer under different conditions. The GDP protein was prepared by incubating with 3× excess GDP; GppNHp protein was prepared by treating 5 units of alkaline phosphatase and 3× excess GppNHp for 4 h at 4 °C. Tris/HCl (50 mM) pH 7.5, 150 mM NaCl, 5 mM $MgCl_2$ and 5 mM dithioerythritol (DTE) was used as buffer throughout. Trimeric complex (human septin complex) was co-expressed in *E. coli* and co-purified using the His and MBP tags on SEPT7 and SEPT2, respectively. SEPT2-315 crystals were grown using 5% polyethylene glycol 6000, 0.1 M bicine pH 9.0, and 0.1 M glycine; crystals were transferred to cryoprotectant containing 25% ethylene glycol along with mother liquor and flash frozen in liquid nitrogen. Selenomethionine-labelled protein was crystallized as above and a SAD data set was used for structure determination. The structure of human septin complex was solved using a combination of five heavy-atom derivatives. All the samples for electron microscopy analysis were incubated in high salt buffer (20 mM HEPES pH 8.0, 800 mM NaCl, 5 mM $MgCl_2$ 10 mM dithiothreitol), except for human septin complex containing the MBP–SEPT2 fusion, which was centrifuged in a glycerol gradient (20 mM HEPES pH 8.0, 600 mM NaCl, 5 mM $MgCl_2$, 5–20% glycerol 5–20%) for 20 h at 92,000*g*. All samples were applied on a single carbon film on an electron microscopy grid and negatively stained with uranyl formate. Class averages of selected particles were reconstructed after reference-free alignment and subsequent MSA and classification. A more detailed description can be found in Methods.

Full Methods and any associated references are available in the online version of the paper at www.nature.com/nature.

Received 10 April; accepted 26 June 2007.
Published online 18 July 2007.

1. Versele, M. & Thorner, J. Some assembly required: yeast septins provide the instruction manual. *Trends Cell Biol.* **15,** 414–424 (2005).
2. Kinoshita, M. The septins. *Genome Biol.* **4,** 236 (2003).
3. Byers, B. & Goetsch, L. A highly ordered ring of membrane-associated filaments in budding yeast. *J. Cell Biol.* **69,** 717–721 (1976).
4. Haarer, B. K. & Pringle, J. R. Immunofluorescence localization of the *Saccharomyces cerevisiae* CDC12 gene product to the vicinity of the 10-nm filaments in the mother-bud neck. *Mol. Cell. Biol.* **7,** 3678–3687 (1987).
5. DeMarini, D. J. *et al.* A septin-based hierarchy of proteins required for localized deposition of chitin in the *Saccharomyces cerevisiae* cell wall. *J. Cell Biol.* **139,** 75–93 (1997).
6. Kozubowski, L. *et al.* A Bni4-Glc7 phosphatase complex that recruits chitin synthase to the site of bud emergence. *Mol. Biol. Cell* **14,** 26–39 (2003).
7. Kinoshita, M. Assembly of mammalian septins. *J. Biochem.* **134,** 491–496 (2003).
8. Macara, I. G. *et al.* Mammalian septins nomenclature. *Mol. Biol. Cell* **13,** 4111–4113 (2002).
9. Hall, P. A., Jung, K., Hillan, K. J. & Russell, S. E. H. Expression profiling the human septin gene family. *J. Pathol.* **206,** 269–278 (2005).
10. Kartmann, B. & Roth, D. Novel roles for mammalian septins: from vesicle trafficking to oncogenesis. *J. Cell Sci.* **114,** 839–844 (2001).
11. Hall, P. A. & Russell, S. E. H. The pathobiology of the septin gene family. *J. Pathol.* **204,** 489–505 (2004).
12. Kuhlenbaumer, G. *et al.* Mutations in SEPT9 cause hereditary neuralgic amyotrophy. *Nature Genet.* **37,** 1044–1046 (2005).
13. Mitchison, T. J. & Field, C. M. Cytoskeleton: What does GTP do for septins? *Curr. Biol.* **12,** R788–R790 (2002).
14. Kinoshita, M., Field, C. M., Coughlin, M. L., Straight, A. F. & Mitchison, T. J. Self- and actin-templated assembly of mammalian septins. *Dev. Cell* **3,** 791–802 (2002).
15. Hsu, S. C. *et al.* Subunit composition, protein interactions, and structures of the mammalian brain sec6/8 complex and septin filaments. *Neuron* **20,** 1111–1122 (1998).
16. Surka, M. C., Tsang, C. W. & Trimble, W. S. The mammalian septin MSF localizes with microtubules and is required for completion of cytokinesis. *Mol. Biol. Cell* **13,** 3532–3545 (2002).
17. Joberty, G. *et al.* Borg proteins control septin organization and are negatively regulated by Cdc42. *Nature Cell Biol.* **3,** 861–866 (2001).
18. Frazier, J. A. *et al.* Polymerization of purified yeast septins — evidence that organized filament arrays may not be required for septin function. *J. Cell Biol.* **143,** 737–749 (1998).
19. Oegema, K., Desai, A., Won, M. L., Mitchison, T. J. & Field, C. M. Purification and assay of a septin complex from *Drosophila* embryos. *Methods Enzymol.* **298,** 279–295 (1998).
20. Field, C. M. *et al.* A purified *Drosophila* septin complex forms filaments and exhibits GTPase activity. *J. Cell Biol.* **133,** 605–616 (1996).
21. Vrabioiu, A. M., Gerber, S. A., Gygi, S. P., Field, C. M. & Mitchison, T. J. The majority of the *Saccharomyces cerevisiae* septin complexes do not exchange guanine nucleotides. *J. Biol. Chem.* **279,** 3111–3118 (2004).
22. Farkasovsky, M., Herter, P., Voss, B. & Wittinghofer, A. Nucleotide binding and filament assembly of recombinant yeast septin complexes. *Biol. Chem.* **386,** 643–656 (2005).
23. Sheffield, P. J. *et al.* Borg/septin interactions and the assembly of mammalian septin heterodimers, trimers, and filaments. *J. Biol. Chem.* **278,** 3483–3488 (2003).
24. Nguyen, T. Q., Sawa, H., Okano, H. & White, J. G. The *C. elegans* septin genes, *unc-59* and *unc-61,* are required for normal postembryonic cytokineses and morphogenesis but have no essential function in embryogenesis. *J. Cell Sci.* **113,** 3825–3837 (2000).
25. Mendoza, M., Hyman, A. A. & Glotzer, M. GTP binding induces filament assembly of a recombinant septin. *Curr. Biol.* **12,** 1858–1863 (2002).
26. Huang, Y. W., Surka, M. C., Reynaud, D., Pace-Asciak, C. & Trimble, W. S. GTP binding and hydrolysis kinetics of human septin 2. *FEBS J.* **273,** 3248–3260 (2006).
27. Leipe, D. D., Wolf, Y. I., Koonin, E. V. & Aravind, L. Classification and evolution of P-loop GTPases and related ATPases. *J. Mol. Biol.* **317,** 41–72 (2002).
28. Scrima, A. & Wittinghofer, A. Dimerisation-dependent GTPase reaction of MnmE: how potassium acts as GTPase-activating element. *EMBO J.* **25,** 2940–2951 (2006).
29. Gasper, R., Scrima, A. & Wittinghofer, A. Structural insights into HypB, a GTP-binding protein that regulates metal binding. *J. Biol. Chem.* **281,** 27492–27502 (2006).
30. Low, C. & Macara, I. G. Structural analysis of septin 2, 6, and 7 complexes. *J. Biol. Chem.* **281,** 30697–30706 (2006).
31. Boehringer, D. *et al.* Three-dimensional structure of a pre-catalytic human spliceosomal complex B. *Nature Struct. Mol. Biol.* **11,** 463–468 (2004).
32. van Heel, M. & Frank, J. Use of multivariate statistics in analysing the images of biological macromolecules. *Ultramicroscopy* **6,** 187–194 (1981).
33. Chant, J. Septin scaffolds and cleavage planes in *Saccharomyces*. *Cell* **84,** 187–190 (1996).
34. Vrabioiu, A. M. & Mitchison, T. J. Structural insights into yeast septin organization from polarized fluorescence microscopy. *Nature* **443,** 466–469 (2006).

Supplementary Information is linked to the online version of the paper at www.nature.com/nature.

Acknowledgements Data collection was done at the Swiss Light Source, beam line X10SA, Paul Scherrer Institute, Villigen, Switzerland, and we thank the beam line staff for assistance. We would like to thank I. Vetter, I. Schlichting, T. Meinhart, W. Blankenfeldt, N. Schrader, E. Hofmann, K. Kühnel, A. Scrima, R. Gasper and R. Rose for data collection and crystallographic advice. M.S. and F.H. thank the International Max Planck Research School for financial support. This work was supported by the 3D Repertoire project, within the EU Sixth Framework Program, and the Fondation Louis-Jeantet.

Author Contributions M.S. purified and crystallized SEPT2-315 and the human septin complex and solved the structures. M.F. made the human septin complex constructs, developed the purification procedure and purified the yeast septin complex used in the electron microscopy. F.H. and H.S. did the electron microscopy analysis. D.K. made SEPT2-315 mutants. M.W. assisted M.S. throughout data collection and structure determination. I.G.M. provided the clones for human septins, and valuable hints. A.W. supervised the project and wrote the paper. All authors discussed the results and commented on the manuscript.

Author Information The atomic coordinates of SEPT2-315 and the human septin complex are deposited in the Protein Data Bank with accession numbers 2QA5 and 2QAG, respectively. Reprints and permissions information is available at www.nature.com/reprints. The authors declare no competing financial interests. Correspondence and requests for materials should be addressed to A.W. (alfred.wittinghofer@mpi-dortmund.mpg.de).

METHODS

Purification and crystallization of SEPT2-315. Wild type and mutant human septin2-315 (amino acids 1–315) were expressed in *E. coli* BL21(DE3) as a GST-fusion protein. After overnight induction at 28 °C, the cell lysate was purified using GSTrap-FF columns (Amersham). SEPT2-315 was cleaved from the tag using PreScission protease and purified using a Superdex S-200 column. The low molecular mass fraction eluted in two peaks with apparent molecular masses of ~72 kDa and ~36 kDa. A large portion eluted in the size exclusion volume as higher oligomers, which was discarded. The monomer–dimer fraction was used for analytical gel filtration described in Methods Summary; the dimer fraction was used for crystallization. Standard buffer used throughout was 50 mM Tris/HCl pH 7.5, 150 mM NaCl, 5 mM $MgCl_2$ and 5 mM DTE. Selenomethionine protein was purified as above using cells grown in minimal media supplemented with selenomethionine.

Twenty milligrams per millilitre protein with 1 mM GDP was used for crystallization. Initial crystallization conditions were obtained by a semi-automatic nanolitre sitting-drop screening using commercial Qiagen/Nextal screening kits, by combining protein and reservoir solution in a 1:1 ratio. Crystallization conditions were optimized by hanging-drop vapour diffusion in 24-well plates at 20 °C. Suitable crystals of SEPT2-315 were obtained in 2 weeks. The reservoir solution contained 5% polyethylene glycol 6000, 0.1 M bicine pH 9.0 and 0.1 M glycine. The crystals were transferred to a cryoprotectant solution containing 25% ethylene glycol together with the mother liquor and immediately flash-frozen in liquid nitrogen. A similar strategy was used to obtain selenomethionine protein crystals, and a SAD data set to 3.4 Å resolution was collected at beam line X10SA Swiss Light Source, Villigen, Switzerland at 100K. Data processing was carried out using the XDS software package[35]. The crystals belonged to space group $C2$ with unit cell dimensions $a = 163$ Å, $b = 54$ Å, $c = 110$ Å, $\alpha = 90°$, $\beta = 128°$, $\gamma = 90°$.

Structure determination of SEPT2-315. SAD data from the selenomethionine protein crystals were used to obtain phases. Eight selenomethionine sites were found using SHELXD[36] and these sites were fed into SOLVE[37] for phase calculation and subsequently RESOLVE[37] for solvent flattening. After a cycle of further density modification using the program DM of the CCP4 package[38], the electron density was used for manual building using COOT[39]. Refinement was done with REFMAC5[40] and the final R_{work} and R_{free} values are 28% and 31.4%, respectively (see Table 1). The final model includes 469 amino acids out of 630 (for dimer), which were residues 20–62, 78–101, 116–139, 141–214, 224–246, 253–268 and 270–304. The model exhibits excellent geometry with 89.4% in favourable, 10.4% in allowed and no residues in disallowed regions of the Ramachandran plot (Supplementary Table 1). Buried surface areas were calculated with CNS[41] using a default probe radius of 1.4 Å.

Purification and crystallization of the human SEPT2–SEPT6–SEPT7 complex. The human septin complex was purified from *E. coli* Rosetta carrying two plasmids as described for recombinant yeast septins[22]. SEPT6 and His–SEPT7 are expressed from a bicistronic vector and MBP–SEPT2 from a second compatible vector. After overnight induction at 28 °C, the human septin complex was purified using Ni-NTA and amylose columns with 25 mM sodium-phosphate pH 7.8, 8% glycerol, 300 mM NaCl, 5 mM $MgCl_2$ and 5 mM β-mercaptoethanol as buffer. Tags were cleaved using thrombin and final purification was via gel filtration using Sephacryl 400 with 20 mM HEPES pH 8.0, 500 mM NaCl, 5 mM $MgCl_2$ and 5 mM DTE as buffer. The hexameric fractions were collected, concentrated by ultrafiltration to 10 mg ml^{-1} and stored at −80 °C. Selenomethionine protein complex was purified as above after growing the cells in minimal media supplemented with selenomethionine. Crystallization trials were done using wild-type human septin complex as well as a mutant in which 57 C-terminal residues of SEPT7 were deleted (human septin complex SEPT7-361). These complexes produced the same elution pattern, crystallized under the same conditions and produced a very similar diffraction pattern.

Crystals of the human septin complex were obtained at 20 °C by the hanging-drop vapour diffusion method with 1.5 µl protein samples mixed with an equal volume of reservoir solution containing 1.4 M ammonium sulphate, 0.1 M Bis-Tris-propane pH 6.5 in 2–3 days. Crystals were collected after a week and transferred to a cryoprotectant solution containing glycerol along with the mother liquor. Transferring the crystals in the cryoprotectant using small gradual steps to a final concentration of 20% glycerol improved the diffraction quality of the crystals. Initial selenomethionine protein crystals were obtained by streak seeding with native crystals and additionally 10 mM TCEP was added to the mother liquor. These initial crystals were used for further micro- and macro-seeding to obtain diffraction quality crystals. Crystals were derivatized with 1–2 mM of the respective heavy atom compounds (see Supplementary Table 3) in the mother liquor over a period of 12–24 h. Several data sets were collected for the native-, selenomethionine- and heavy-atom-soaked crystals at beam line X10SA SLS, Villigen, Switzerland at 100K. Crystals exhibited a high degree of anisotropy. Data processing was done using the XDS software package[35]. Crystals belong to the $P4_322$ space group with unit cell constants $a = b = 252$ Å, $c = 156$ Å, $\alpha = \beta = \gamma = 90°$ with a solvent content of 72% and Matthews' coefficient of 4.3 Å^3 Da^{-1} (estimated for one hexamer per asymmetric unit).

Structure determination of the human septin complex. Initial phases were obtained using SOLVE[37] and RESOLVE[37] from selenomethionine crystals. The program identified only 16 sites out of 82 (expected for one hexamer) and the resultant electron density looked like a tube mesh. Similar output was seen for Ta_6Br_{14} crystals with one cluster per asymmetric unit. These weak phases were used for the cross validation of selenomethionine and Ta_6Br_{14} phases and were also used to calculate an anomalous Fourier map from the SAD data sets collected from di-µ-iodobis(ethylenediamine) diplatinum(II) nitrate (PIP)-, $HgCl_2$- and K_2PtCl_4-soaked crystals (Supplementary Table 3). The sites were hand-picked manually and fed into SOLVE for phase calculation using the MIRAS approach with five derivatives along with native, which gave good experimental phases up to 5.5 Å, and the resultant electron density after RESOLVE showed the secondary structural elements (Supplementary Fig. 3a).

In another approach, molecular replacement was performed with the native 4 Å data using MOLREP[38] and a monomeric poly-alanine structure of SEPT2 as a search model. The resultant replacement solution contained three monomers where the trimeric model from MOLREP fitted very well with the experimentally phased electron density (Supplementary Fig. 3b), supporting the notion that a trimer not a hexamer occupies the asymmetrical unit. The crystals thus have an unusually high solvent content of 85.7% and Matthews' coefficient of 8.7 Å^3 Da^{-1}.

In order to identify the position of each individual polypeptide, we used the information provided by selenomethionine, as the three septins contain different numbers of methionines in different positions of the polypeptide chain (Supplementary Fig. 1). The locations of SEPT2, SEPT6 and SEPT7 in the asymmetrical unit could be unequivocally identified (Fig. 2a). The initial trimeric model (molecular replacement output) was used to generate phases and the model-derived phases were combined with experimental phases and extended to 4 Å. CNS[41] composite omit maps were generated to locate the missing parts. After several cycles of rebuilding, a model was generated where SEPT2 was taken from the SEPT2 G-dimer model, SEPT6 and SEPT7 were built using manual guidance by the replacement model and the methionine positions, side chains were placed confidently around the methionine positions, and the rest was built as poly-alanine stretches because the side chains were not visible. Initial refinement was done without nucleotide; where positive density was observed in the nucleotide-binding regions, nucleotides were placed in those densities and included in the final refinement. Refinement was done using REFMAC[40] with translation, libration, screw-rotation displacement (TLS) refinement, and the final R_{work} and R_{free} values were 37.5% and 39.2%, respectively (Table 1). Ramachandran statistics were obtained using PROCHECK (http://www.biochem.ucl.ac.uk/~roman/procheck/procheck.html). $F_o - F_c$ maps shown in Fig. 2c were calculated by removing the nucleotide from the respective subunit. Figures were generated using PYMOL[42].

Electron microscopy. Human septin complex was incubated in high salt buffer (20 mM HEPES pH 8.0, 800 mM NaCl, 5 mM $MgCl_2$ 10 mM dithiothreitol). Human septin complex containing the MBP–SEPT2 fusion construct was centrifuged in a glycerol gradient (20 mM HEPES pH 8.0, 600 mM NaCl, 5 mM $MgCl_2$, glycerol 5–20%) for 20 h at 92,000g and 4 °C. After centrifugation and fractionation, samples were fixed in 0.05% glutaraldehyde to stabilize the complex and to obtain images suitable for image processing. Because complex formation capacity in the MBP–SEPT2 fusion complex is reduced, centrifugation and fixation at slightly lowered salt was necessary to obtain stable hexameric septin complexes. High salt conditions without gradient centrifugation and chemical stabilization did result in fragmentation of septin complexes containing the MBP–SEPT2 fusion complex. Lower salt conditions without gradient centrifugation and chemical stabilization, on the other hand, yielded a highly heterogeneous complex population (data not shown). The human septin complex lacking the coiled coils (ΔCC) and yeast septin complex consisting of Cdc3–Cdc10–Cdc11–Cdc12 was prepared for electron microscopy as described for the unmodified human septin complex. All samples were applied on a single carbon film on an electron microscopy grid covered with carbon support film (containing 1–4 µm holes) and negatively stained with uranyl formate. Low-dose images were taken on a 4k × 4k CCD camera in a Philips CM200 FEG electron microscope. Images of the yeast septin complex were recorded in a Philips CM120 electron microscope. Class averages of selected particles were computed after alignment by classification[43] and subsequent rounds of multivariate statistical analysis[44] and classification[45], and multi-reference alignment[46]. The average number of members per class was 40 images. Most (~80%) particles were intact hexamers. Within the data sets, 10–20% of class averages containing

non-hexameric complexes were detected, which can be attributed to a remaining heterogeneous subpopulation of complexes and to flexibility of the SEPT2–SEPT6–SEPT7 complex. For image processing, IMAGIC-5 software was used[47]. Image alignment was done by exhaustive alignment using re-sampling to polar coordinates[46]. For particle statistics see Supplementary Table 4.

35. Kabsch, W. Automatic processing of rotation diffraction data from crystals of initially unknown symmetry and cell constants. *J. Appl. Cryst.* **26,** 795–800 (1993).
36. Schneider, T. R. & Sheldrick, G. M. Substructure solution with SHELXD. *Acta Crystallogr. D* **58,** 1772–1779 (2002).
37. Terwilliger, T. C. SOLVE and RESOLVE: automated structure solution and density modification. *Methods Enzymol.* **374,** 22–37 (2003).
38. CCP4. The CCP4 (Collaborative Computational Project Number 4) suite: programs for protein crystallography. *Acta Crystallogr. D* 50 760–763 (1994).
39. Emsley, P., &. Cowtan, K. Coot: Model-building tools for molecular graphics. *Acta Crystallogr. D* 60 2126–2132 (2004).
40. Murshudov, G. N., Vagin, A. A. & Dodson, E. J. Refinement of macromolecular structures by the maximum-likelihood method. *Acta Crystallogr. D* **53,** 240–255 (1997).
41. Brunger, A. T. *et al.* Crystallography & NMR system: A new software suite for macromolecular structure determination. *Acta Crystallogr. D* 54 905–921 (1998).
42. DeLano, W. L. The PyMOL Molecular Graphics System ⟨http://www.pymol.org⟩ (2006).
43. Dube, P., Tavares, P., Lurz, R. & van Heel, M. The portal protein of bacteriophage SPP1: a DNA pump with 13-fold symmetry. *EMBO J.* **12,** 1303–1309 (1993).
44. van Heel, M. & Frank, J. Use of multivariate statistics in analysing the images of biological macromolecules. *Ultramicroscopy* **6,** 187–194 (1981).
45. van Heel, M. Classification of very large electron microscopical image data sets. *Opik* **82,** 114–126 (1989).
46. Sander, B., Golas, M. M. & Stark, H. Corrim-based alignment for improved speed in single-particle image processing. *J. Struct. Biol.* **143,** 219–228 (2003).
47. van Heel, M., Harauz, G., Orlova, E. V., Schmidt, R. & Schatz, M. A new generation of the IMAGIC image processing system. *J. Struct. Biol.* **116,** 17–24 (1996).